Universal Scaling of the Minimum Error Probability in Qualification of Quantum States

Zhaoyu Fei, Yaotian Li, Weicheng Huang, and Xiaoguang Wang*
Zhejiang Key Laboratory of Quantum State Control and Optical Field Manipulation, Department of Physics, Zhejiang Sci-Tech University, 310018 Hangzhou, China

Y. M. Du†
Graduate School of China Academy of Engineering Physics, Beijing 100193, China

(Dated: August 11, 2026)

Qualification of quantum states judges which of two sets of quantum states an unknown state lies in, where the two sets are labeled by two distinct parameter regions. We formulate this problem as a composite quantum hypothesis test and uncover universal scaling laws for the minimum error probability for N copies. Taking polarization-direction qualification and purity qualification as examples, we show that the N-copy permutation symmetry and the geometric symmetries of the parameter regions identify the optimal measurements and the "worst pairwise states". The minimum error probability scales as $N^{-3/2}\exp(-N\xi)$ for disjoint regions and as $(NF)^{-1/2}$ for adjacent regions, where ξ and F are the quantum Chernoff divergence and quantum Fisher information associated with the "worst pairwise states", respectively. With the minimum error probability serving as an order parameter, the transition between the scaling behaviors becomes a second-order phase transition as $N \to \infty$. Our approach determines whether a quantum state belongs to a given set without full state tomography, thereby enabling qualification of large ensembles using finite samples.

Introduction.— As quantum technologies progress from proof-of-principle demonstrations to practical implementations, a critical task is to judge whether experimentally prepared ensembles meet prescribed requirements, using only finite measurement resources. In this context, many quantum technologies do not require a source to produce a unique ideal state. Instead, its output parameters need to lie within a prescribed tolerance window [1], defined as the set of parameter values deemed acceptable for the intended operation. Such tolerance windows arise naturally in quantum technologies. Single-photon sources are assessed using thresholds on multiphoton suppression, indistinguishability, brightness, and mode quality [2–6]. Quantum sensors and clocks require squeezing or metrological gain above classical benchmarks [7–14]. Finite-sample quantum metrology asks whether a parameter encoded in a quantum state lies within a prescribed tolerance window [1]. Quantum communication requires polarized photons transmitted through optical fibers to remain within an admissible angular region despite fiber-induced polarization diffusion [15–20].

While these platforms employ different acceptance criteria, a unified statistical framework for judging whether an unknown state lies within the corresponding admissible parameter region is still unestablished. Such a framework is needed to account for finite-sample fluctuations, calibration drift, device imperfections, and to assess device reliability, including aging and operational lifetime [21–23].

In this Letter, we formulate the problem of qualifying an unknown quantum state according to prescribed acceptance criteria as a quantum composite hypothesis test. Two representative examples are considered: polarization-direction qualification (PDQ) and purity qualification (PQ). For both examples, the derivation exploits the permutation symmetry of the N copies and the geometric symmetries of the parameter regions, namely $U(1)$ symmetry for PDQ and $SO(3)$ symmetry for PQ, to identify the optimal measurements and the worst pairwise states. These states minimize the quantum Chernoff divergence over two state sets [24]. The relative configuration of the windows then gives rise to three universal finite-N scaling laws for the minimum error probability $P_{\mathrm{e}}^{\min}$. For disjoint regions, $P_{\mathrm{e}}^{\min} \propto N^{-3/2}\exp(-N\xi)$; for adjacent regions, $P_{\mathrm{e}}^{\min} \propto (NF)^{-1/2}$; and for overlapping regions, $P_{\mathrm{e}}^{\min}$ converges to a nonzero intrinsic value as $N \to \infty$. Here, ξ and F are, respectively, the quantum Chernoff divergence [25] and quantum Fisher information [26–30] associated with the worst pairwise states. Furthermore, in the $N \to \infty$ limit, $P_{\mathrm{e}}^{\min}$ serves as the order parameter for a second-order transition between the disjoint- and overlapping-region phases, with the adjacent-region configuration marking the critical point. Unlike quantum state tomography, which reconstructs the full state [31–38], qualification of quantum states extracts only the relevant information and can therefore require fewer samples.

Qualification of quantum states.— Consider a quantum source with an output state $\rho_{\boldsymbol{\theta}}$, where $\boldsymbol{\theta} \in \Theta$. Qualification of quantum states partitions the parameter space Θ into an admissible region Θ_0 and a rejected region Θ_1, thereby defining two hypotheses, $H_0 : \boldsymbol{\theta} \in \Theta_0$, $H_1 : \boldsymbol{\theta} \in \Theta_1$. These hypotheses are tested using a binary positive-operator-valued measure (POVM) $\{E_0, E_1\}$, with $E_0 + E_1 = \mathbb{1}$ and $E_i \geq 0$, where outcome

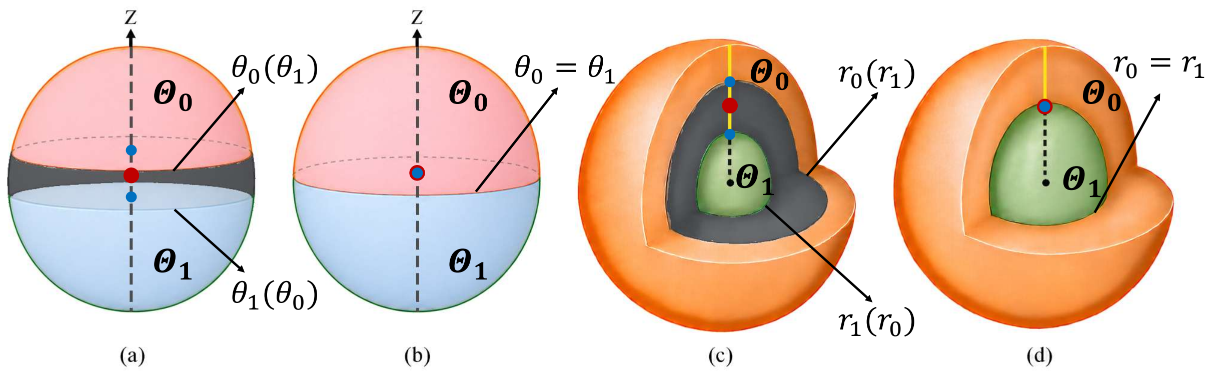

Fig. 1. Schematic illustration of the region configurations for PDQ and PQ. Panels (a) and (b) show PDQ, whereas panels (c) and (d) show PQ. The gray domains in panels (a) and (c) have different meanings. For disjoint regions, they denote domains in which no state under consideration lies (for overlapping regions, they denote the intersections $\Theta_0 \cap \Theta_1$). Panels (b) and (d) show adjacent regions. In panels (a) and (b), the orange and green surface domains denote Θ_0 and Θ_1, while the pink and light-blue interior domains denote the convex hulls of the corresponding state sets. In panels (c) and (d), the orange and green domains denote Θ_0 and Θ_1, respectively. In panel (c), the yellow line marks an arbitrary radius of the Bloch ball. In all panels, blue dots mark the worst pairwise states, and the red dot marks the cutoff state.

i judges that H_i holds [25].

Because states associated with Θ_0 are generally nonorthogonal to those associated with Θ_1, perfect discrimination is impossible. A type-I error occurs when $\boldsymbol{\theta} \in \Theta_0$ is assigned to H_1, whereas a type-II error occurs when $\boldsymbol{\theta} \in \Theta_1$ is assigned to H_0. To reduce these errors, we use N independent and identically prepared copies and optimize the POVM. Specifically, for a prior distribution $\mathrm{d}\mu(\boldsymbol{\theta})$ supported on Θ, the Bayesian error probability is

$$P_{\mathrm{e}} = \sum_{i=0}^{1} \int_{\Theta_i} \mathrm{Tr}\left[\rho_{\boldsymbol{\theta}}^{\otimes N} E_{1-i}\right] \mathrm{d}\mu(\boldsymbol{\theta}). \tag{1}$$

The optimal measurement is obtained by minimizing P_{e} over all binary POVMs. Introducing $\rho_i = \pi_i^{-1} \int_{\Theta_i} \rho_{\boldsymbol{\theta}}^{\otimes N} \mathrm{d}\mu(\boldsymbol{\theta})$, with $\pi_i = \int_{\Theta_i} \mathrm{d}\mu(\boldsymbol{\theta})$, the task reduces to binary state discrimination between ρ_0 and ρ_1 with priors π_0 and π_1. This optimization gives the minimum error probability [25, 26, 39]

$$P_{\mathrm{e}}^{\min} = \frac{1}{2}\left[1 - \|\pi_1\rho_1 - \pi_0\rho_0\|_1\right], \tag{2}$$

where $\|\cdot\|_1$ denotes the trace norm. The optimal POVM is obtained according to the eigenspaces of $\pi_1\rho_1 - \pi_0\rho_0$: E_1 projects onto its positive eigenspace and E_0 onto its negative eigenspace. The zero eigenspace may be arbitrarily assigned to E_0 or E_1.

Since the effective states ρ_0 and ρ_1 are defined by integrals of $\rho_{\boldsymbol{\theta}}^{\otimes N}$ over parameter regions, deriving the spectral decomposition of $\pi_1\rho_1 - \pi_0\rho_0$ and the corresponding optimal POVM in closed form is generally difficult. We therefore exploit the symmetries shared by the regions and the prior distribution: these symmetries fix the structure of the optimal measurement and enable an analytic evaluation of the minimum error probability. We next illustrate this construction with two examples.

Polarization-direction qualification and purity qualification.— We first consider the PDQ for a spin-1/2 state $|\psi\rangle$. The spin-1/2 state is parametrized by the Bloch-sphere angles $\boldsymbol{\theta} = (\theta, \phi)$ as $|\psi\rangle = \cos\frac{\theta}{2}|1/2\rangle + \mathrm{e}^{i\phi}\sin\frac{\theta}{2}|-1/2\rangle$, where $|1/2\rangle$ and $|-1/2\rangle$ denote the states polarized along the $+z$ and $-z$ directions, respectively. Choosing $+z$ as the target direction, the qualification is to judge whether the unknown direction lies within the prescribed angular regions, i.e.,

$$\begin{aligned} \Theta_0^{\mathrm{PDQ}} &= \{(\theta,\phi) : 0 \le \theta \le \theta_0,\ 0 \le \phi < 2\pi\}, \\ \Theta_1^{\mathrm{PDQ}} &= \{(\theta,\phi) : \theta_1 \le \theta \le \pi,\ 0 \le \phi < 2\pi\}, \end{aligned} \tag{3}$$

where the boundaries θ_0 and θ_1 define polar caps that are invariant under rotations about the z axis (the corresponding window configurations are illustrated in Fig. 1a and 1b). The prior distribution is chosen to share this $U(1)$ symmetry, i.e., $\mathrm{d}\mu(\theta,\phi) = q(\cos\theta)\sin\theta \mathrm{d}\theta\mathrm{d}\phi$ for some smooth density function q.

For PDQ, the permutation symmetry among the N copies and the $U(1)$ symmetry of the parameter regions jointly determine the optimal measurement. Specifically, the permutation symmetry restricts the effective states ρ_0 and ρ_1 to the totally symmetric subspace of the N-copy Hilbert space $\mathcal{H}_{1/2}^{\otimes N}$, with total spin number $S_{\max} = N/2$. Moreover, the $U(1)$ symmetry further renders $\pi_1\rho_1 - \pi_0\rho_0$ diagonal in the Dicke basis $\{|S_{\max}, M\rangle\}$, where M is the magnetic quantum number. The remaining subspaces can be arbitrarily assigned to E_0 or E_1, since $\pi_1\rho_1 - \pi_0\rho_0$ has zero eigenvalues on them. This freedom reduces the Dicke-basis measurement to an equivalent local implementation: each spin is measured along the z direction, and the judgment is made from the total magnetization.

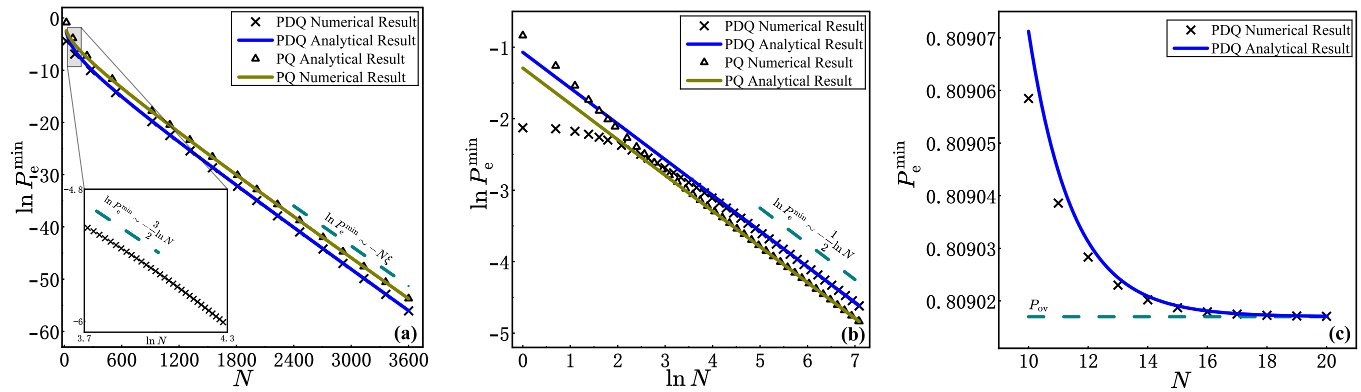

Fig. 2. Numerical verification of the minimum error probability for PDQ and PQ. (a) Disjoint regions, with $\theta_0 = 0.05\pi$, $\theta_1 = 0.15\pi$ for PDQ and $r_0 = 0.9$, $r_1 = 0.72$ for PQ. (b) Adjacent regions, with $\theta_0 = \theta_1 = 0.15\pi$ for PDQ and $r_0 = r_1 = 0.35$ for PQ. (c) Overlapping regions for PDQ, with $\theta_0 = 0.8\pi$ and $\theta_1 = 0.2\pi$. Crosses ($\times$) and triangles ($\triangle$) denote the numerical results for PDQ and PQ, respectively, obtained by Eq. (1), whereas solid curves show the analytical results from Eq. (6). Gray dashed lines indicate the asymptotic scaling laws in panels (a) and (b) and the intrinsic error probability in panel (c). The inset in panel (a) highlights the $N^{-3/2}$ scaling in the small-N regime.

Guided by the symmetry analysis above, we parametrize the POVM by cutoff angle x [40] as

$$E_0^{\rm PDQ}(x) = \sum_{M=S_{\max}\cos x+1}^{S_{\max}} |\boldsymbol{S}\rangle_{M\,M}\langle \boldsymbol{S}|, \tag{4}$$

where $|\boldsymbol{S}\rangle_M = |s_1\rangle \otimes \cdots \otimes |s_N\rangle$ denotes a product state in the z basis, with $s_k \in \{1/2, -1/2\}$ constrained by $M = \sum_{k=1}^{N} s_k$. Substituting Eq. (4) into Eq. (1) gives the x-dependent error probability $P_{\rm e}(x)$. The minimizer x_* is then obtained from $\mathrm{d}P_{\rm e}(x)/\mathrm{d}x = 0$ (see Supplemental Material [41] for details), yielding

$$x_* = \begin{cases} \arccos\left[\dfrac{\ln(\sin\theta_1) - \ln(\sin\theta_0)}{\ln\left(\tan\frac{\theta_1}{2}\right) - \ln\left(\tan\frac{\theta_0}{2}\right)}\right], & \theta_0 \neq \theta_1, \\ \theta_0, & \theta_0 = \theta_1. \end{cases} \tag{5}$$

Substituting Eq. (5) into $P_{\rm e}(x)$ gives

$$P_{\rm e}^{\min} \simeq \begin{cases} A_{\rm s} N^{-3/2} \mathrm{e}^{-N\xi}, & \theta_0 < \theta_1, \\ A_{\rm b}\,[NF]^{-1/2}, & \theta_0 = \theta_1, \\ P_{\rm ov} + A_{\rm s} N^{-3/2}\mathrm{e}^{-N\xi}, & \theta_0 > \theta_1. \end{cases} \tag{6}$$

where $A_{\rm s}$ and $A_{\rm b}$ are N-independent prefactors given in Supplemental Material [41] (when the prior density vanishes at the boundary, the scaling laws of minimum error probability are modified [42]). The three lines correspond to disjoint, adjacent, and overlapping regions, respectively. For disjoint regions, the exponential decay is characterized by the Chernoff exponent ξ [24], which is given by

$$\xi = D(t_*\|t_0) = D(t_*\|t_1) = C(t_0\|t_1), \tag{7}$$

where $t_i = \cos^2(\theta_i/2)$, $t_* = \cos^2(x_*/2)$, $D(a\|b) = a\ln(a/b) + (1-a)\ln[(1-a)/(1-b)]$ and $C(a\|b) = -\ln\inf_{0<s<1}\left[a^s b^{1-s} + (1-a)^s(1-b)^{1-s}\right]$ are respectively the Kullback–Leibler (KL) divergence and the Chernoff divergence between two Bernoulli distributions [43–45]. In the third equality of Eq. (7), we have used the relation between the KL divergence and the Chernoff divergence [46]. For adjacent regions, the exponential decay is replaced by a power law. As $t_1 \to t_0$, $C(t_0\|t_1) \sim F(t_0 - t_1)^2/8$, where $F = 1/[t_0(1-t_0)]$ is the Fisher information of the Bernoulli distribution entering Eq. (6). For overlapping regions, the intersection $\Theta_0 \cap \Theta_1$ carries the prior weight [47] and $P_{\rm ov} = \pi_0 + \pi_1 - 1$, which gives a nonzero intrinsic error probability as $N \to \infty$. The Chernoff exponent ξ also governs the finite-N correction to this limit.

We next consider the PQ for a qubit state ρ. The qubit state is parametrized by the Bloch-vector $\mathbf{r} = (r_x, r_y, r_z)$ as $\rho = (\mathbb{1} + \mathbf{r}\cdot\boldsymbol{\sigma})/2$, where $0 \le r \le 1$ and $\boldsymbol{\sigma} = (\sigma_x, \sigma_y, \sigma_z)$ is the vector of Pauli matrices. Since the purity of ρ is $\mathrm{Tr}(\rho^2) = (1 + r^2)/2$, the qualification is to judge whether the Bloch radius r lies within the prescribed radial tolerance in spherical coordinates on the Bloch ball, i.e.,

$$\begin{aligned} \Theta_0^{\rm PQ} &= \{(r,\theta,\phi) : r_0 \le r \le 1,\ 0 \le \theta \le \pi,\ 0 \le \phi < 2\pi\}, \\ \Theta_1^{\rm PQ} &= \{(r,\theta,\phi) : 0 \le r \le r_1,\ 0 \le \theta \le \pi,\ 0 \le \phi < 2\pi\}, \end{aligned} \tag{8}$$

where r_0 and r_1 denote the radial boundaries. The regions defined by these boundaries are invariant under arbitrary rotations of the Bloch vector (the corresponding windows configurations is illustrated in Fig. 1c and 1d). The prior distributions are chosen to share this $SO(3)$ symmetry, i.e., $\mathrm{d}\mu(r,\theta,\phi) = w(r) r^2 \sin\theta\, \mathrm{d}r\, \mathrm{d}\theta \mathrm{d}\phi$, for some smooth density function w.

For the PQ, the N-copy state remains permutation invariant, but the $U(1)$ symmetry about the z-axis is enlarged to $SO(3)$ rotational symmetry about the Bloch vector. As in the PDQ, these two symmetries determine the structure of $\pi_1\rho_1 - \pi_0\rho_0$: it is constant on each block labeled by the total angular momentum S, with the constant λ_S. More explicitly, Schur–Weyl duality gives the decomposition $\mathcal{H}_{1/2}^{\otimes N} = \bigoplus_S \mathcal{V}_S \otimes \mathcal{K}_S$, which together with Schur's lemma leads to $\pi_1\rho_1 - \pi_0\rho_0 = \bigoplus_S \lambda_S \left(\mathbb{1}_{\mathcal{V}_S} \otimes \mathbb{1}_{\mathcal{K}_S}\right)$. Here $\mathcal{V}_S$ carries the irreducible $SU(2)$ repres entation with total angular momentum S, while $\mathcal{K}_S$ is the multiplicity space carrying the corresponding irreducible representation of the symmetric group $\mathcal{S}_N$.

Guided by the symmetry analysis above, we parametrize the POVM by a cutoff x [40] as

$$E_0^{\mathrm{PQ}}(x) = \bigoplus_{S=xS_{\max}+1}^{S_{\max}} \left(\mathbb{1}_{\mathcal{V}_S} \otimes \mathbb{1}_{\mathcal{K}_S}\right). \tag{9}$$

Substituting Eq. (9) into Eq. (1) gives the x-dependent error probability $P_{\mathrm{e}}(x)$. Applying a minimization procedure similar to that used for the PDQ yields the minimizer x_* and the minimum error probability for all three types of region configurations. Their expressions take the same forms as in Eqs. (5) and (6), with t_i and t_* now redefined as $t_i = (1+r_i)/2$ and $t_* = (1+x_*)/2$. The explicit prefactors are given in Supplemental Material [41].

These two examples exhibit universal scaling of the minimum error probability: despite differences in their prior distributions, symmetries, and optimal measurements, both exhibit the three types of scaling laws summarized in Eq. (6). In Fig. 2, we further compare the numerical results obtained by minimizing the error probability defined in Eq. (1) with the analytical asymptotic expressions in Eq. (6) for both qualification tasks under the three types of region configurations. Their agreement at large N supports the predicted universal scaling. The reference dashed lines indicate the $N^{-3/2}$ prefactor and the $\exp(-N\xi)$ decay in panel (a), the $N^{-1/2}$ scaling in panel (b), and the intrinsic error probability in panel (c).

Worst pairwise states and phase transition.—The worst pairwise states, denoted by $\rho_{\mathrm{w},0}$ and $\rho_{\mathrm{w},1}$, are a pair of states that attain the minimum quantum Chernoff divergence over all pairs belonging to two sets of quantum states, $\rho \in \mathcal{C}_0$ and $\sigma \in \mathcal{C}_1$, where the quantum Chernoff divergence is defined as $C_{\mathrm{Q}}(\rho\|\sigma) = -\ln \min_{0\le s\le 1} \mathrm{Tr}\left(\rho^s\sigma^{1-s}\right)$ [24, 25, 48]. When the two worst pairwise states approach each other through a parameter, i.e., $\rho_{\mathrm{w},0} = \rho_\alpha$ and $\rho_{\mathrm{w},1} = \rho_{\alpha+\mathrm{d}\alpha}$, the leading variation of the quantum Chernoff divergence is $C_{\mathrm{Q}}\left(\rho_\alpha\|\rho_{\alpha+\mathrm{d}\alpha}\right) \sim F_{\mathrm{Q}}\left(\rho_\alpha\right)(\mathrm{d}\alpha)^2/8$ [49], where $F_{\mathrm{Q}}(\rho_\alpha) = \mathrm{Tr}\left(\rho_\alpha L_\alpha^2\right)$ is the quantum Fisher information with respect to the parameter α and L_α is the symmetric logarithmic derivative defined by $\partial\rho_\alpha/\partial\alpha = \left(\rho_\alpha L_\alpha + L_\alpha\rho_\alpha\right)/2$ [30, 50, 51].

We next use the worst pairwise states to reveal the intrinsic connection between the geometric symmetry and the universal scaling of the minimum error probability. In the PDQ, the two sets of quantum states are the convex hulls [52] of the state families associated with the parameter regions in Eq. (3), $\mathcal{C}_i = \mathrm{conv}\{\rho_{\boldsymbol{\theta}} : \boldsymbol{\theta} \in \Theta_i\}$. The $U(1)$ symmetry of $\mathcal{C}_0$ and $\mathcal{C}_1$ restricts the search for the worst pairwise states to the z axis. Among the corresponding intersection points, the pair minimizing the quantum Chernoff divergence gives the worst pairwise states shown in Fig. 1(a). Their density matrices are diagonal in the S_z basis, $\rho_{\mathrm{w},i} = \mathrm{diag}\left[t_i, 1-t_i\right]$, where $t_i = \cos^2(\theta_i/2)$. Their quantum Chernoff divergence therefore coincides with the Chernoff divergence between two Bernoulli distributions in Eq. (7). The relation derived above between the KL divergence and the Chernoff divergence has a quantum counterpart: $C_{\mathrm{Q}}\left(\rho_{\mathrm{w},0}\|\rho_{\mathrm{w},1}\right) = D_{\mathrm{Q}}\left(\rho_{x_*}\|\rho_{\mathrm{w},0}\right) = D_{\mathrm{Q}}\left(\rho_{x_*}\|\rho_{\mathrm{w},1}\right)$, where $D_{\mathrm{Q}}(\rho\|\sigma) = \mathrm{Tr}[\rho(\ln\rho - \ln\sigma)]$ is the quantum relative entropy [53]. Here, the cutoff state (marked by the red dot in Fig. 1a) is diagonal in the S_z basis, $\rho_{x_*} = \mathrm{diag}[t_*, 1-t_*]$ with x_* given by Eq. (5), where $t_* = \cos^2(x_*/2)$. For the adjacent-region configuration, the three states coincide, $\rho_{\mathrm{w},0} = \rho_{\mathrm{w},1} = \rho_{x_*}$, as shown in Fig. 1(b), of which the quantum Fisher information reproduces the Fisher information of the Bernoulli distribution in Eq. (6). For the overlapping-region configuration, the minimum error probability approaches a nonzero intrinsic value.

In the PQ, the two sets of quantum states are taken as the quantum states associated with the parameter regions in Eq. (8), $\mathcal{C}_i = \{\rho_{\boldsymbol{\theta}} : \boldsymbol{\theta} \in \Theta_i\}$. The $SO(3)$ symmetry makes all radial directions of the Bloch ball equivalent. For the disjoint- and adjacent-region cases, the density matrices of worst pairwise states are the pair of intersections of any chosen radius with $\mathcal{C}_0$ and $\mathcal{C}_1$ that minimizes the quantum Chernoff divergence, as shown in Fig. 1(c) and 1(d). In the basis aligned with the chosen radius, the worst pairwise states in the PQ have the same diagonal structure as those in the PDQ, except that t_i and t_* are now redefined as $t_i = (1+r_i)/2$ and $t_* = (1+r_*)/2$. The preceding analysis therefore yields analogous results for the Chernoff divergence and the Fisher information in Eqs. (6) and (7).

The three types of scaling laws in Eq. (6) reveal a phase transition characterized by the signed distance $d = \epsilon\xi$. Here, ϵ takes values -1, 0, and 1 for disjoint, adjacent, and overlapping regions, respectively. The adjacent-region case then marks the critical point. For PDQ near the critical point, $P_{\mathrm{ov}}/\sqrt{\xi}$, ξA_{s}, and the prefactor A_{b} in Eq. (6) depend only on the cutoff angle x_* (see Supplemental Material [41] for details). To eliminate this nonuniversal dependence, we impose $\theta_0+\theta_1 = \pi$, thereby fixing $x_* = \pi/2$. Figure 3(a) shows $P_{\mathrm{e}}^{\min}$ as a function

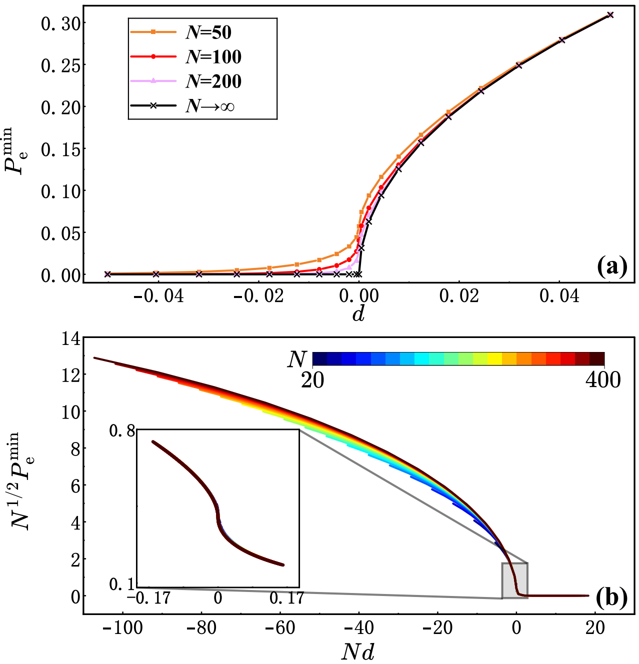

Fig. 3. Finite-N scaling analysis of the minimum error probability in the PDQ. (a) Minimum error probability $P_{\mathrm{e}}^{\min}$ as a function of signed distance for N copies. (b) For N copies, with N from $N=20$ to $N=400$, the rescaled error probability $N^{1/2}P_{\mathrm{e}}^{\min}$ is plotted as a function of d.

of d for several copy numbers N. As N increases, the transition from the disjoint-region phase ($d<0$) to the overlapping-region phase ($d>0$) becomes sharper, with $P_{\mathrm{e}}^{\min}$ as an order parameter that remains finite in the overlapping-region phase and vanishes in the disjoint-region phase. This behavior is consistent with a second-order transition in the large-N limit. In Fig. 3(b), we plot $N^{1/2}P_{\mathrm{e}}^{\min}$ as a function of Nd for copy numbers from $N=20$ to $N=400$ and observe a collapse near the critical point, which is described by the finite-N scaling form

$$P_{\mathrm{e}}^{\min}(N,d,x_*) = N^{-1/2}g(x_*)f(Nd), \tag{10}$$

where $g(x_*)$ is a prefactor determined by the prior distribution, while $f(Nd)$ is a scaling function.

Discussions.—Previous work in composite quantum hypothesis testing has reduced the Chernoff exponent governing the minimum error probability for discriminating two quantum-state sets to the Chernoff divergence between their worst pairwise states, typically assuming commuting or quasi-classical state families, or convex state sets [54–59]. The parameter regions considered here generally violate these assumptions: the corresponding sets of quantum states are nonconvex in the state space, and states drawn from the competing regions can be both noncommuting and nonorthogonal. Nevertheless, by exploiting the permutation symmetry of the N copies and the geometric symmetries of the parameter regions, we reduce the Chernoff exponent to the Chernoff divergence between the worst pairwise states and identify these states via the symmetries of the state sets. This reduction therefore extends beyond the previous commuting, quasi-classical, and convex settings.

To illustrate the application of the theory, consider photons with horizontal (H) or vertical (V) polarization are disturbed during the long-distance transmission in optical fiber. We aim to qualify photon polarization using PDQ. Let γ denote the ratio of the transmission distance to the polarization-diffusion length of the optical fiber [60–62], with $\gamma<\ln 2$, $\gamma=\ln 2$, and $\gamma>\ln 2$ corresponding to the disjoint-, adjacent-, and overlapping-region cases in PDQ, respectively. For $\gamma<\ln 2$, our result suggests that achieving an error probability ϵ requires a detected photon number $N_{\mathrm{req}}\simeq 2\ln\epsilon/\ln\left[1-(2\exp(-\gamma)-1)^2\right]$, while $\gamma=\ln 2$ corresponds to the maximum fiber transmission distance over which photon polarizations remain distinguishable, beyond which an intrinsic error prevents the qualification error probability from being made arbitrarily small by increasing the photon number.

Acknowledgments.—This work was supported by the Science Challenge Project (Grant No. TZ2025017) , the Quantum Science and Technology-National Science and Technology Major Project (Grant No. 2024ZD 0301000) , the National Natural Science Foundation of China (Grant No. 12405046), and the Science Foundation of Zhejiang Sci-Tech University (Grants No. 23062088-Y and No. 23062181-Y).

* xgwang@zstu.edu.cn
† ymdu@gscaep.ac.cn

[1] J. J. Meyer, S. Khatri, D. Stilck França, J. Eisert, and P. Faist, PRX Quantum **6**, 030336 (2025).
[2] C. Santori, D. Fattal, J. Vučković, G. S. Solomon, and Y. Yamamoto, Nature **419**, 594 (2002).
[3] N. Somaschi, V. Giesz, L. De Santis, J. Loredo, M. P. Almeida, G. Hornecker, S. L. Portalupi, T. Grange, C. Anton, J. Demory, *et al.*, Nature Photonics **10**, 340 (2016).
[4] X. Ding, Y. He, Z.-C. Duan, N. Gregersen, M.-C. Chen, S. Unsleber, S. Maier, C. Schneider, M. Kamp, S. Höfling, *et al.*, Physical review letters **116**, 020401 (2016).
[5] P. Lodahl, S. Mahmoodian, and S. Stobbe, Rev. Mod. Phys. **87**, 347 (2015).
[6] P. Senellart, G. Solomon, and A. White, Nat. Nanotechnol. **12**, 1026 (2017).
[7] C. M. Caves, Phys. Rev. D **23**, 1693 (1981).
[8] D. J. Wineland, J. J. Bollinger, W. M. Itano, F. L. Moore, and D. J. Heinzen, Phys. Rev. A **46**, R6797 (1992).
[9] M. Kitagawa and M. Ueda, Phys. Rev. A **47**, 5138 (1993).
[10] V. Giovannetti, S. Lloyd, and L. Maccone, Science **306**, 1330 (2004).
[11] V. Giovannetti, S. Lloyd, and L. Maccone, Nat. Photonics **5**, 222 (2011).

[12] C. L. Degen, F. Reinhard, and P. Cappellaro, Rev. Mod. Phys. **89**, 035002 (2017).

[13] L. Pezzè, A. Smerzi, M. K. Oberthaler, R. Schmied, and P. Treutlein, Rev. Mod. Phys. **90**, 035005 (2018).

[14] R. Schnabel, Phys. Rep. **684**, 1 (2017).

[15] C. B. Czegledi, M. Karlsson, E. Agrell, and P. Johannisson, Sci. Rep. **6**, 21217 (2016).

[16] M. B. Willemsen, M. U. F. Khalid, M. P. van Exter, and J. P. Woerdman, Phys. Rev. Lett. **82**, 4815 (1999).

[17] P. K. A. Wai and C. R. Menyuk, Opt. Lett. **19**, 1517 (1994).

[18] P. K. A. Wai and C. R. Menyuk, Opt. Lett. **20**, 2493 (1995).

[19] P. K. A. Wai and C. R. Menyuk, J. Lightwave Technol. **14**, 148 (1996).

[20] T. Imai and T. Matsumoto, Opt. Lett. **12**, 723 (1987).

[21] L. X. Cui, Y.-M. Du, and C. P. Sun, Phys. Rev. Lett. **131**, 160203 (2023).

[22] Y. Li, Y.-M. Du, W. Ding, Z. Fei, L. Fu, and X. Wang, Phys. Rev. A **112**, 032220 (2025).

[23] M.-M. Yi, L. X. Cui, Y.-M. Du, and C. P. Sun, Phys. Rev. A **113**, 062613 (2026).

[24] M. Mosonyi, Z. Szilágyi, and M. Weiner, IEEE Trans. Inf. Theory **68**, 1032 (2022).

[25] K. M. R. Audenaert, J. Calsamiglia, R. Muñoz Tapia, E. Bagan, L. Masanes, A. Acin, and F. Verstraete, Phys. Rev. Lett. **98**, 160501 (2007).

[26] C. W. Helstrom, J. Stat. Phys. **1**, 231 (1969).

[27] A. S. Holevo, *Probabilistic and Statistical Aspects of Quantum Theory* (Springer Basel, 2011).

[28] M. Hübner, Phys. Lett. A **179**, 226 (1993).

[29] J. Ma and X. Wang, Phys. Rev. A **80**, 012318 (2009).

[30] J. Liu, H. Yuan, X.-M. Lu, and X. Wang, J. Phys. A: Math. Theor. **53**, 023001 (2019).

[31] D. F. V. James, P. G. Kwiat, W. J. Munro, and A. G. White, Phys. Rev. A **64**, 052312 (2001).

[32] J. B. Altepeter, E. R. Jeffrey, and P. G. Kwiat, in *Adv. At. Mol. Opt. Phys.*, Vol. 52 (Academic Press, 2005) pp. 105–159.

[33] D. Gross, Y.-K. Liu, S. T. Flammia, S. Becker, and J. Eisert, Phys. Rev. Lett. **105**, 150401 (2010).

[34] M. Cramer, M. B. Plenio, S. T. Flammia, R. Somma, D. Gross, S. D. Bartlett, O. Landon-Cardinal, D. Poulin, and Y.-K. Liu, Nat. Commun. **1**, 149 (2010).

[35] S. T. Flammia and Y.-K. Liu, Phys. Rev. Lett. **106**, 230501 (2011).

[36] M. P. da Silva, O. Landon-Cardinal, and D. Poulin, Phys. Rev. Lett. **107**, 210404 (2011).

[37] S. Pallister, N. Linden, and A. Montanaro, Phys. Rev. Lett. **120**, 170502 (2018).

[38] J. Eisert, D. Hangleiter, N. Walk, I. Roth, D. Markham, R. Parekh, U. Chabaud, and E. Kashefi, Nat. Rev. Phys. **2**, 382 (2020).

[39] S. M. Barnett and S. Croke, Adv. Opt. Photon. **1**, 238 (2009).

[40] Throughout, a lower bound of the form $y+1$ denotes the smallest admissible quantum number strictly larger than y on the relevant integer or half-integer lattice.

[41] Detailed derivations of the optimal measurement, the asymptotic error probabilities, and additional results for purity qualification will be provided in a forthcoming Supplemental Material.

[42] In deriving Eq. (6), we have assumed that $q(\cos\theta)$ is finite and nonzero at the boundaries θ_0 and θ_1. If instead $q(\cos\theta) \sim |\cos\theta - \cos\theta_i|^\alpha$ with $\alpha > 1$, the scaling behavior become $N^{-3/2-\alpha}\exp(-N\xi)$ and $(NF)^{-(1+\alpha)/2}$.

[43] H. Chernoff, Ann. Math. Stat. **23**, 493 (1952).

[44] M. Hellman and J. Raviv, IEEE Trans. Inf. Theory **16**, 368 (1970).

[45] R. Blahut, IEEE Trans. Inf. Theory **20**, 405 (1974).

[46] F. Nielsen, Entropy **24**, 1400 (2022).

[47] The prior distribution $d\mu(\boldsymbol{\theta})$ is normalized on $\Theta_0 \cup \Theta_1$. For disjoint regions, $\pi_0 + \pi_1 = 1$, so the π_i can be interpreted as prior probabilities. For overlapping regions, the intersection $\Theta_0 \cap \Theta_1$ contributes to both π_0 and π_1, giving $\pi_0 + \pi_1 = 1 + \mu(\Theta_0 \cap \Theta_1) > 1$. Therefore, π_i are referred to as prior weights rather than Bayesian priors.

[48] C. A. Fuchs, arXiv (1996), arXiv:quant-ph/9601020 [quant-ph].

[49] J. Calsamiglia, R. Muñoz Tapia, L. Masanes, A. Acin, and E. Bagan, Phys. Rev. A **77**, 032311 (2008).

[50] M. Nussbaum and A. Szkoła, Ann. Stat. **37**, 1040 (2009).

[51] S. L. Braunstein and C. M. Caves, Phys. Rev. Lett. **72**, 3439 (1994).

[52] For each region Θ_i, the convex hull $\mathcal{C}_i = \mathrm{conv}\{\rho_{\boldsymbol{\theta}} : \boldsymbol{\theta} \in \Theta_i\}$ contains all convex mixtures $\sum_k p_k \rho_{\boldsymbol{\theta}_k}$, where $\boldsymbol{\theta}_k \in \Theta_i$, $p_k \geq 0$, and $\sum_k p_k = 1$.

[53] F. Hiai and D. Petz, Commun. Math. Phys. **143**, 99 (1991).

[54] M. Berta, F. G. S. L. Brandão, and C. Hirche, Commun. Math. Phys. **385**, 55 (2021).

[55] M. Mosonyi, Z. Szilágyi, and M. Weiner, IEEE Trans. Inf. Theory **68**, 1032 (2022).

[56] L. Lami, IEEE Trans. Inf. Theory **71**, 4454 (2025).

[57] L. Lami, arXiv (2025), arXiv:2510.06340 [quant-ph].

[58] K. Fang and M. Hayashi, arXiv (2025), arXiv:2508.12889 [quant-ph].

[59] J. P. Simpson, E. Palias, and S. T. Jose, arXiv (2026), arXiv:2601.08588 [quant-ph].

[60] A. Galtarossa, L. Palmieri, M. Schiano, and T. Tambosso, Opt. Lett. **25**, 384 (2000).

[61] A. Galtarossa, L. Palmieri, M. Schiano, and T. Tambosso, Opt. Lett. **26**, 962 (2001).

[62] M. A. Eronyan, D. R. Devetyarov, A. A. Reutskiy, A. A. Untilov, S. M. Aksarin, I. K. Meshkovskiy, M. A. Bisyarin, and A. A. Pechenkin, Mater. Lett. **301**, 130316 (2021).